$Pr_{0.5}Sr_{0.5-x}Ba_xMnO_3$: Size and Mismatch Effects on Structural and Magnetic Transitions

C. Autret, C. Martin,* M. Hervieu, A. Maignan, and B. Raveau

Laboratoire CRISMAT, associé au CNRS, UMR6508, ISMRA, 6 Boulevard du Maréchal Juin, 14050 CAEN Cedex, France

G. André and F. Bourée

Laboratoire Léon Brillouin, CEA Saclay, 91191 GIF sur YVETTE Cedex, France

Z. Jirak

Institute of Physics ACSR, Cukrovarnicka 10, 162 53 PRAGUE 6, Czech Republic

Received October 23, 2002. Revised Manuscript Received January 27, 2003

The structural and magnetic transitions in the $Pr_{0.5}Sr_{0.5-x}Ba_xMnO_3$ series have been investigated by neutron diffraction and electron microscopy, in connection with the transport and magnetic properties, allowing a new phase diagram (T, x, or $<r_A>$) to be drawn. Two important points emerge from this study. First, a phase separation is observed for a large part of the diagram, described as a mixture of ferromagnetic, antiferromagnetic, and poorly ordered magnetic phases at low temperature for $x > 0.2$. Second, A-type antiferromagnetism (AFM) develops in nearly regular perovskite lattice. The case of $Pr_{0.5}Ba_{0.5}MnO_3$ is also discussed because its microstructure is not conventional with local cationic ordering in the random A-site matrix.

Introduction

The half-doped perovskite manganites $Ln_{0.5}AE_{0.5}MnO_3$ (Ln is a trivalent lanthanide and AE is a divalent alkaline-earth) have been the subject of numerous studies. Depending on the Ln and AE cations, these compounds exhibit different structural and magnetic states versus temperature. One of the most investigated systems is that based on Pr, due to its low-temperature antiferromagnetic (AFM) state that was reported earlier as charge- and orbital-ordered of CE-type (in Wollan and Koehler notation) for AE = Ca and only orbital-ordered of A-type for AE = Sr.[1,2] The (Pr,Ca) manganites were mainly studied for this particular charge ordered state[3,4] and the (Pr,Sr) one was studied for its magnetoresistive properties.[5,6]

The change from one structural and magnetic type to the other was investigated for the $Pr_{0.5}Sr_{0.5-x}Ca_xMnO_3$ series showing a decisive role of the average A-site cation size ($<r_A>$) in the structural and physical properties of this complex system.[7,8] An important point about this series was the discovery of the best magnetoresistive (MR) properties for $Pr_{0.5}Sr_{0.41}Ca_{0.09}MnO_3$ situated close to the boundary between the CE and A-type AFM ground states.[9−11]

In the present paper, we propose to continue this investigation toward still larger average A-site cationic size by studying the $Pr_{0.5}Sr_{0.5-x}Ba_xMnO_3$ series. First, there is a very little knowledge concerning the half-doped manganites characterized by large $<r_A>$,[12,13] probably due to the stability of different polytypes related to hexagonal perovskite structure.[14,15] Second, the substitution of barium for strontium not only increases the average A-site cation size but also increases the disorder induced by the difference between the Sr and Ba sizes lying on the same A-site and quantified by the variance $\sigma^2 = \Sigma y_i r_i^2 - <r_A>^2$. This parameter is well-known to have a drastic effect on the behavior of the manganites.[16−18] We report herein on

* To whom correspondence should be addressed via E-mail: christine.martin@ismra.fr.

(1) Wollan, E. O.; Koehler, W. C. *Phys. Rev.* **1955**, *100*, 545.
(2) Goodenough, J. B. *Phys. Rev.* **1955**, *100*, 564.
(3) Jirak, Z.; Krupicka, S.; Simsa, Z.; Dlouha, M.; Vratislav, S. *J. Magn. Magn. Mater.* **1985**, *53*, 153.
(4) Mori, S.; Katsufuji, T.; Yamamoto, N.; Chen, C. H.; Cheong, S.−W. *Phys. Rev. B* **1999**, *59*, 13573.
(5) Tomioka, Y.; Asamitsu, A.; Moritomo, Y.; Kuwahara, H.; Tokura, Y. *Phys. Rev. Lett.* **1995**, *74*, 5108.
(6) Kawano, H.; Kajimoto, R.; Yoshizawa, H.; Tomioka, Y.; Kuwahara, H.; Tokura, Y. *Phys. Rev. Lett.* **1997**, *78*, 4253.
(7) Damay, F.; Martin ,C.; Maignan, A.; Hervieu, M.; Raveau, B.; Jirak, Z.; André, G.; Bourée, F. *Chem. Mater.* **1999**, *11*, 536.
(8) Krupicka, S.; Marysko, M.; Jirak, Z.; Hejtmanek, J. *J. Magn. Mater.* **1999**, *206*, 45.
(9) Wolfman, J.; Simon, C.; Hervieu, M.; Maignan ,A.; Raveau, B. *J. Solid State Chem.* **1996**, *123*, 413.
(10) Damay, F.; Jirak, Z.; Hervieu, M.; Martin, C.; Maignan, A.; Raveau, B.; André, G.; Bourée, F. *J. Magn. Magn. Mater.* **1998**, *190*, 221.
(11) Jirak, Z.; Damay, F.; Hervieu, M.; Martin ,C.; Raveau, B.; André, G.; Bourée, F. *Phys. Rev. B* **2000**, *61*, 1181.
(12) Woodward, P. M.; Vogt ,T.; Cox, D. E.; Arulraj, A.; Rao, C. N. R.; Karen, P.; Cheetham, A. K. *Chem. Mater.* **1998**, *10*, 3652.
(13) Rao, C. N. R.; Arulraj, A.; Santosh ,P. N.; Cheetham, A. K. *Chem. Mater.* **1998**, *10*, 2714.
(14) Chamberland, B. L.; Sleight, A. W.; Weiher, J. F. *J. Solid State Chem.* **1970**, *1*, 506.
(15) Negas, T.; Roth, R. S. *J. Solid Sate Chem.* **1971**, *3*, 323.
(16) Rodriguez-Martinez, L. M.; Attfield, J. P. *Phys. Rev. B* **1996**, *54*, R15622.
(17) Attfield, J. P. *Chem. Mater.* **1998**, *10*, 3239.

10.1021/cm020474s CCC: $25.00
Published on Web 04/05/2003

detailed neutron diffraction and electron microscopy investigations of $Pr_{0.5}Sr_{0.5-x}Ba_xMnO_3$ compounds ($x = 0-0.5$), complemented by measuring their magnetic and transport properties.

Experimental Procedure

The $Pr_{0.5}Sr_{0.5-x}Ba_xMnO_3$ compounds (with $x = 0$, 0.05, 0.2, 0.3, 0.4, and 0.5) were prepared by solid-state reaction at high temperature. Homogenized mixtures of Pr_6O_{11}, $SrCO_3$, $BaCO_3$, and MnO_2, in the amount of 10 g, were calcinated twice at 950 °C to achieve decarbonation. The powders were then pressed into pellets and heated at 1500 °C for 12 h in air for the compositions corresponding to $x \leq 0.2$. For $x > 0.2$, this synthesis resulted in occurrence of hexagonal phases, and, consequently, a new two-step preparation was adopted. The samples were heated in argon flow, first up to 1200 °C for 12 h and then to 1500 °C for 12 h. Finally, the pellets were annealed at 600 °C under oxygen pressure ($PO_2 = 100$ bar) during 24 h. Equivalence of both procedures (air and argon firing with subsequent oxygenation) was checked with $x = 0.2$ composition. First structural characterization of the products was done by X-ray diffraction at room temperature with a Philips diffractometer using the Cu Kα radiation.

Neutron experiments were carried out at the LLB (Saclay, France) on the G41 diffractometer using a wavelength $\lambda = 2.4266$ Å to determine crystalline and magnetic structures versus temperature. Samples were first cooled to helium temperature and patterns were recorded over an angular range $17° < 2\theta < 97°$ by warming from 1.5 K to room temperature by 5-K steps. Additional patterns, using the high-resolution diffractometer 3T2 with a wavelength $\lambda = 1.2251$ Å, were collected at room temperature and 10 K in the range $6° < 2\theta < 125.7°$. Data were refined by the Rietveld method using the program Fullprof.[19]

The electron diffraction (ED) study was carried out with a JEOL 200CX electron microscope equipped with a tilt-rotation goniometer (±60°). The ED study versus temperature down to 92 K was carried out with a JEOL 2010 electron microscope. The high-resolution microscopy study was carried out with a TOPCON 002B microscope (working at 200 kV, with a point resolution of 1.8 Å). The reconstructions of the reciprocal space coupled with EDS analyses were systematically performed on numerous grains. They confirmed the homogeneity of the cationic distribution in the crystals, in agreement with the nominal compositions.

Magnetization measurements were performed with a vibrating sample magnetometer in a magnetic field of 10^{-2} T or 1.45 T, by increasing the temperature from 4 to 300 K after a zero field cooling. Magnetoresistance measurements were done with a Quantum Design physical property measurements system. The resistivity was measured on bars, with dimensions $0.2 \times 0.2 \times 1$ cm^3, using a standard four-point method. All the ρ(T) curves were measured with decreasing temperature, from 400 to 5 K, in zero magnetic field or under 7 T.

Results

Neutron diffraction studies, electron microscopy characterizations, and magnetotransport properties were carried out for the entire series. For clarity, the results are detailed in different sections due to the complexity of the system and to the numerous investigations.

I. Magnetic Properties of the $Pr_{0.5}Sr_{0.5-x}Ba_xMnO_3$ Series. For the $0 \leq x \leq 0.2$ compounds, magnetization curves (M(T)) registered in 10^{-2} T (Figure 1) exhibit a bell shape. With decreasing temperature, the samples show two transitions, from paramagnetic (PM) to ferromagnetic (FM) at T_C and then toward AFM at T_N. The curves in Figure 1 exhibit, for x increasing from 0 to 0.2, a common transition from PM to a bulk FM with decreasing T_C. For $x \geq 0.3$ the transition is gradual, but T_C increases suddenly at $x = 0.3$ and only one broad transition from PM to FM is observed. In this x range, the M(T) curves recorded in 1.45 T (inset of Figure 1) confirm the FM character but they also show that a pure FM state is not obtained. The M maximum is not observed for the lower temperature, for instance in the $x = 0.3$ case, the magnetization value reaches only ≈1.3 μ_B at 4 K, whereas the maximal M value is obtained around 120 K with ≈1.7 μ_B, which is far from the theoretical one (3.5 μ_B), suggesting the existence of AFM interactions.

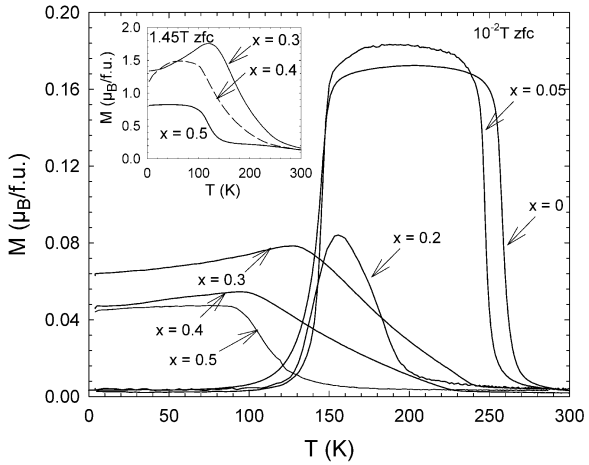

Figure 1. $Pr_{0.5}Sr_{0.5-x}Ba_xMnO_3$ magnetization curves recorded in 10^{-2} T (zfc), the x values are given on the graph. In inset are also shown the M (T) curves registered in 1.45 T (zfc) for the larger x samples.

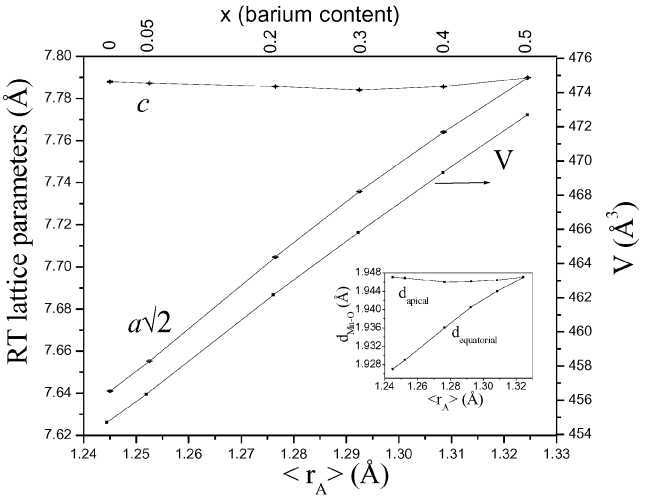

Figure 2. Dependence on $<r_A>$ (bottom x-axis) of the room-temperature lattice parameters (left y-axis) and volume (right y-axis) of the $Pr_{0.5}Sr_{0.5-x}Ba_xMnO_3$ series (from 3T2 NPD data); the x dependence (top x-axis) is also given. The Mn−O distances versus $<r_A>$ are given in the inset.

II. Neutron Diffraction Study of the $Pr_{0.5}Sr_{0.5-x}Ba_xMnO_3$ Series. *II.1. Room Temperature (RT) Structural Investigation, from High-Resolution (3T2) Data.* At RT, the $Pr_{0.5}Sr_{0.5-x}Ba_xMnO_5$ compounds with $x = 0$, 0.05, 0.2, 0.3, and 0.4 are in the PM state and the neutron powder diffraction (NPD) patterns are indexed

(18) Damay, F.; Martin, C.; Maignan, A.; Raveau, B. *J. Appl. Phys.* **1997**, *82*, 6181.

(19) Rodriguez-Carjaval, J. In *Collected Abstracts of Powder Diffraction Meeting 1990*; Galy, J., Ed.; Toulouse, France.

Table 1. $Pr_{0.5}Sr_{0.5-x}Ba_xMnO_3$: Crystallographic Parameters Obtained from RT Neutron Diffraction Data (3T2) and Selected Interatomic Distances and Angles

x	0[a]	0.05	0.2	0.3	0.4	0.5
space group	*I*4/*mcm*	*I*4/*mcm*	*I*4/*mcm*	*I*4/*mcm*	*I*4/*mcm*	*Pm*3*m*
$<r_A>$ (Å)	1.245	1.2525	1.2765	1.2925	1.3085	1.3245
σ^2 (Å^2)	4.29 10^{-3}	6.554 10^{-3}	12.5 10^{-3}	15.9 10^{-3}	18.8 10^{-3}	21.1 10^{-3}
a (Å)	5.4031(1)	5.41393 (2)	5.44822 (4)	5.47020 (6)	5.49263 (5)	3.89491 (3)
c (Å)	7.7879(2)	7.78735 (6)	7.78579 (7)	7.78425 (9)	7.7857 (1)	3.89491 (3)
V (Å^3)	227.3	228.2	231.2	232.9	234.9	59.09 (= 236.4)
Pr, Sr, Ba (site 4b)						(site 1a)
x	0	0	0	0	0	0
y	0.5	0.5	0.5	0.5	0.5	0
z	0.25	0.25	0.25	0.25	0.25	0
B (Å^2)	0.54 (2)	0.61 (1)	0.59 (1)	0.55 (1)	0.52 (1)	0.52 (1)
Mn (site 4c)						(site 1b)
x	0	0	0	0	0	0.5
y	0	0	0	0	0	0.5
z	0	0	0	0	0	0.5
B (Å^2)	0.16 (3)	0.23 (2)	0.25 (2)	0.28 (2)	0.24 (2)	0.33 (2)
O_{apical} (site 4a)						(site 3c)
x	0	0	0	0	0	0.5
y	0	0	0	0	0	0.5
z	0.25	0.25	0.25	0.25	0.25	0
B (Å^2)	1.08 (3)	1.28 (2)	1.47 (2)	1.58 (3)	1.71 (6)	1.65 (1)
$O_{equatorial}$ (site 8h)						
x	0.7832 (12)	0.78141 (8)	0.77513 (8)	0.7705 (1)	0.7633 (1)	
y	0.2832 (12)	0.28141 (8)	0.27513 (8)	0.2705 (1)	0.2633 (1)	
z	0	0	0	0	0	
B (Å^2)	0.83 (2)	1.01 (1)	1.29 (1)	1.47 (1)	1.59 (3)	
R_{Bnuc} %		2.84	3.34	3.40	2.84	3.30
R_{wp}	7.27	7.83	7.93	8.61	9.59	10.3
X^2	2.66	3.66	3.64	2.05	3.09	2.19
Mn−O_{ap} (Å) (× 2)	1.947(1)	1.9468(1)	1.9464(1)	1.9461(1)	1.9464(1)	1.947
Mn−O_{eq} (Å) (× 4)	1.927(1)	1.9292(4)	1.9360(5)	1.9405(6)	1.945(09)	
Mn−O_{ap}−Mn (°)	180.0	180.0	180.0	180.0	180.0	180.0
Mn−O_{eq}−Mn (°)	164.80(4)	165.66(2)	168.51(2)	170.61(3)	173.86(3)	

[a] The $x = 0$ results are from reference 20.

in a quadruple cell with $a_p\sqrt{2} \times a_p\sqrt{2} \times 2a_p$ (a_p is the cell parameter of the ideal perovskite) with the *I*4/*mcm* space group.[20] The cell volume increases with x, in agreement with the Ba size, larger than the Sr one.[21] Note however that c remains nearly constant, whereas a increases, as shown in Figure 2. This x dependence of the lattice parameters leads finally to a cubic cell for the $x = 0.5$ compound (space group *Pm*3*m* with $a = 3.894$ Å). It is worth mentioning that the increase of a parameter cannot be associated solely with the gradual change of the Mn−O−Mn angles toward the ideal 180° but is largely due to an increase of equatorial Mn−O distances, keeping at the same time the apical Mn−O distances constant (see inset of Figure 2). As a result, the size of MnO_6 octahedra slightly increases, which should be related to a change of internal stress in the perovskite structure with $<r_A>$. Starting from the elongated MnO_6 octahedra observed for $Pr_{0.5}Sr_{0.5}MnO_3$, the equatorial Mn−O distances increase monotonically with x, leading to regular octahedra for $Pr_{0.5}Ba_{0.5}MnO_3$. The structural results from RT high-resolution NPD data are summarized in Table 1. Note that the oxygen content is refined to "$O_{3.00}$" in all cases. Nevertheless, if the B factors of cations remain nearly constant vs x, these factors increase with x (from 0 to 0.4, i.e., in the *I*4/*mcm* space group) for O_1 and O_2 atoms. Let us note that refinement of anisotropic factors does not allow significant improvement of the fit.

II.2. Low-Temperature (LT) Structural Study from 3T2 Data. For clarity, the results obtained for the $Pr_{0.5}Ba_{0.5}MnO_3$ sample will be given separately, at the end of the section. At 10 K, all the compounds for $0 \le x < 0.5$ exhibit an A-type AFM component associated with a *Fmmm* crystalline structure.[20] In such a structure, FM planes are antiferromagneticaly coupled.[1,2] A-type AFM alone is observed for $x = 0$, 0.05, and 0.2, but for larger x values a FM component is added, retaining the *I*4/*mcm* space group (same as evidenced for these compounds at RT). These results are provided in Figure 3 and Table 2. The *Fmmm* cell volume increases regularly with x (lower panel of Figure 3) at the same rate as observed at RT. The cell distortion evolves slightly from $x = 0$ to 0.3, that is in the monophasic area, and then suddenly (for $x > 0.3$) this distortion, associated with the A-type AFM phase, decreases (upper panel). For the $x = 0.3$ compound, where a mixture of FM (*I*4/*mcm*) and AFM (*Fmmm*) is observed in the approximative ratio $^2/_3$:$^1/_3$, the FM cell is more regular than the AFM one but its volume is slightly larger than the one of the AFM cell. For $x = 0.4$, where AFM and FM are refined roughly in the ratio $^1/_2$:$^1/_2$, both cell parameter sets are similar. As will be discussed in the following section, the ND data refinements for such interconnected multiphase states are rather delicate. It is particularly true in the case of an important coincidence between the cell parameters of the tetragonal and

(20) Damay, F.; Martin, C.; Hervieu, M.; Maignan, A.; Raveau, B.; André, G.; Bourée, F. *J. Magn. Magn. Mater.* **1998**, *184*, 71.
(21) Shannon, R. D.; Prewitt, C. T. *Acta Crystallogr. B* **1976**, *25*, 925.

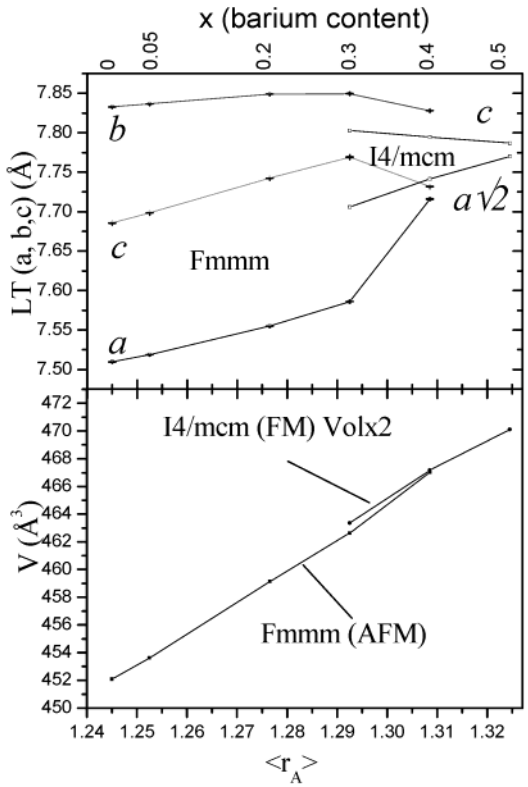

Figure 3. Dependence on $<r_A>$ (bottom *x*-axis) and *x* (top *x*-axis) of the low-temperature lattice parameters (upper panel) and corresponding cell volume evolution (lower panel), from 3T2 NPD data refinements. The I-type cell volume is multiplied by 2, to be compared with the F-type one.

orthorhombic phases, leading to high agreement factors at low temperature for some samples of the series (Table 2). Moreover, for the $x = 0.3$ compound that exhibits the higher agreement factors, an additional parameter has to be taken into account, with a large "stress parameter" refined for the *I*4/*mcm* phase (not given in the tables). This point will also be mentioned in the electron microscopy section. The quality of the refinements is exemplified by Figure 4a which gives the experimental and calculated plots for $x = 0.4$. From the magnetic point of view, the 3T2−10 K pattern refinements lead, through the entire series, to an A-type AFM structure with the AFM interactions along *x* and the moment along *y* for $x = 0$ to 0.2, and then for $x = 0.3$ and 0.4 it rotates in the *(y, z)* plane. For the latter (i.e., $x = 0.3$ and 0.4) that also exhibit FM at LT ($T_C > T_N$), the FM component is evidenced along *z*, whatever the temperature: no reorientation is observed in the FM state at T_N. The more puzzling point is the suppression of the characteristic orthorhombic distortion in the A-type AFM phase for the $x = 0.4$ compound (Table 2). Confirmed by the electron microscopy study (see section III), the pseudotetragonal metrics of the *Fmmm* cell ($a \sim c$) probably originates from a nonhomogeneous LT state in which the FM and AFM regions are microscopically intertwinned. The coexistence of two phases at LT is a usual observation in manganites that fits in with the phase-separated scenario proposed for such perovskites.[22,23] The stress imposed by one domain on the others does not allow the lattice distortion to develop.[24] Despite this, the A-type AFM order is long range and the refined moments are large (2.58 μ_B), suggesting that an appreciable $d_{x^2-y^2}$ orbital polarization is still present.

The $x = 0.5$ compound exhibits a different 3T2-LT pattern. From the magnetic point of view, like the $x = 0.3$ and 0.4 samples, it shows a mixture of FM and AFM states. This LT data refinement is different from the others because it is made by using a unique crystalline *I*4/*mcm* phase associated with two magnetic ones (FM + AFM). Let us underline that, compared with previous compositions, it is possible that this compound also exhibits at LT a mixture of *I*4/*mcm* and *Fmmm* but with cell parameters too close to be differentiated on the NPD patterns. Moreover, as shown in Figure 4b, the peaks characteristic of the A-type AFM are broad. By combining the 3T2 and G41 data, the LT state can be described by a FM component, established at long range (the moment is refined to 1.46 μ_B and is along *z*), and by an A-type AFM one, that is only at short range. The calculated coherence length for the AFM is ≈45 Å with a refined moment of 1.64 μ_B along *z*, but because of the pseudocubic structure and the poorly ordered magnetic state, the refinement did not allow determination of the value and the orientation of the moment with accuracy. The average moment per Mn site detected in $Pr_{0.5}Ba_{0.5}MnO_3$ by the neutron diffraction ($\sqrt{(1.46^2 + 1.64^2)} = 2.20$ μ_B) is significantly smaller than that expected for a complete order. Consequently, the LT nonhomogeneous state of this sample can be described as roughly $^1/_4$ FM, $^1/_4$ A-AFM, and $^1/_2$ magnetically disordered. Thus, it is clear that the strain phenomena previously discussed for $x = 0.4$ are accentuated for the $x = 0.5$ sample because of its nearly cubic structure. In fact, there is a weak tetragonal distortion and the MnO_6 octahedra are slightly distorted, and the Mn−O distances are calculated to 1.944 and 1.947 Å.

II.3. *Structural and Magnetic Evolution versus Temperature (from G41 Data).* The $x = 0.05$ and 0.2 compounds exhibit similar temperature dependence, as previously described for $x = 0$.[20] This is illustrated with the evolution of the structural and magnetic parameters for $x = 0.05$ (Figure 5), and the NPD patterns for $x = 0.2$ (Figure 6). Starting from the room-temperature paramagnetic phase of the *I*4/*mcm* symmetry, by decreasing *T*, a first magnetic transition is evidenced at T_C (≈250 K and 180 K, for $x = 0.05$ and 0.2, respectively). This *I*4/*mcm* structure and the associated FM component disappear with the onset of the *Fmmm* phase associated with an A-type AFM structure at T_N (≈150 and 140 K, respectively).

For $x = 0.3$ and 0.4, the temperature dependence is more complex. As shown in Figure 7, for the $x = 0.4$ sample, by the temperature dependence of the intensity of magnetic peaks and by the evolution of the NPD patterns (inset), the transitions are smoother and the distortions are less pronounced at LT than previously observed for smaller *x* compounds. In fact, by decreasing the temperature from RT, a FM component appears around 190 K without any structural transition and develops progressively down to ≈105 K and then

(22) Mori, S.; Chen, C. H.; Cheong, S.-W. *Phys. Rev. Lett.* **1998**, *81*, 3972.
(23) Moreo, A.; Yunoki, S.; Dagotto, E. *Science* **1999**, *283*, 2034.
(24) Amelinckx, S., Gevers, R., Van Landuyt, J., Eds. *Diffraction and Imaging Techniques in Material Sciences*; North-Holland: Amsterdam, The Netherlands.

Table 2. $Pr_{0.5}Sr_{0.5-x}Ba_xMnO_3$: Crystallographic Parameters Obtained from 10 K Neutron Diffraction Data (3T2) and Selected Interatomic Distances and Angles

x	0[a]	0.05	0.2	0.3		0.4		0.5
$<r_A>$ (Å)	1.245	1.2525	1.2765	1.2925		1.3085		1.3245
σ^2 (Å^2)	4.29 10^{-3}	6.554 10^{-3}	12.5 10^{-3}	15.9 10^{-3}		18.8 10^{-3}		21.1 10^{-3}
space group	*Fmmm*	*Fmmm*	*Fmmm*	*Fmmm*	*I*4/*mcm*	*Fmmm*	I4/*mcm*	I4/*mcm*
a (Å)	7.5095 (1)	7.51864 (5)	7.55505 (7)	7.5844 (2)	5.44845 (9)	7.7157 (2)	5.47402 (9)	5.49429 (6)
b (Å)	7.8329 (2)	7.83675 (5)	7.84912 (7)	7.8495 (2)	5.44845 (9)	7.8285 (2)	5.47402 (9)	5.49429 (6)
c (Å)	7.6857 (2)	7.69854 (6)	7.7424 (1)	7.7706 (2)	7.8047 (2)	7.7320 (2)	7.7953 (2)	7.7868 (1)
V (Å^3)	452.0	453.6	459.1	462.6	231.7	467.0	233.6	235.1
Pr, Sr, Ba, (site 8h)					(site 4b)			
x	0	0	0	0	0	0	0	0
y	0.250 (2)	0.2509 (1)	0.2505 (2)	0.249 (1)	0.5	0.251 (1)	0.5	0.5
z	0	0	0	0	0.25	0	0.25	0.25
B (Å^2)	0.20 (2)	0.21 (1)	0.25 (1)	0.33 (3)	0.33 (3)	0.25 (1)	0.25 (1)	0.36 (3)
Mn (site 8d)					(site 4c)			
x	0.25	0.25	0.25	0.25	0	0.25	0	0
y	0	0	0	0	0	0	0	0
z	0.25	0.25	0.25	0.25	0	0.25	0	0
B (Å^2)	0.02 (3)	0.04 (2)	0.05 (2)	0.09 (3)	0.09 (3)	0.17 (2)	0.17 (2)	0.34 (4)
O_{picol} (site 8f)					(site 4a)			
x	0.25	0.25	0.25	0.25	0	0.25	0	0
y	0.25	0.25	0.25	0.25	0	0.25	0	0
z	0.25	0.25	0.25	0.25	0.25	0.25	0.25	0.25
B (Å^2)	0.58 (2)	0.68 (5)	0.96 (2)	1.0 (1)	1.24 (7)	1.31 (5)	1.27 (7)	1.53 (1)
$O1_{equatorial}$ (site 8g)					(site 8h)			
x	0.213 (1)	0.2149 (1)	0.2197 (2)	0.2250 (7)	0.7762 (3)	0.2298 (6)	0.7682 (3)	0.7584 (3)
y	0	0	0	0	0.2762 (3)	0	0.2682 (3)	0.2584 (3)
z	0	0	0	0	0	0	0	0
B (Å^2)	0.55 (2)	0.63 (2)	0.89 (2)	1.05 (11)	1.10 (4)	0.86 (8)	1.27 (4)	1.71 (8)
$O2_{equatorial}$ (site 8i)								
x	0	0	0	0		0		
y	0	0	0	0		0		
z	0.288 (2)	0.2865 (1)	0.2814 (2)	0.2764 (7)		0.2757 (8)		
B (Å^2)	0.45 (2)	0.54 (1)	0.73 (2)	0.80 (8)		1.69 (9)		
M (AFM [010] or [011])	3.4	3.26 (1)	3.18 (2)	3.35 (5)		2.58 (4)		1.64 (5)
M (FM//z)					2.55 (6)		2.560 (8)	1.46 (5)
phase %				35	65	52	48	
R_{Bnuc} %		2.36	3	7.1	4.13	3.12	2.93	3.3
$R_{Bmagn.}$ %		3.18	3.02	11.8	4.35	14	5.3	11.6(AF)/4.3(F)
R_p	5.8	7.43	8.73	15.5		9.74		10.9
R_{wp}	6.8	7.7	9.82	15.8		8.45		12.7
X^2	2.15	3.12	4.67	6.9		2.4		6
Mn−O_{ap} (Å) (× 2)	1.958	1.9592(1)	1.9623(1)	1.9624(1)	1.9512(1)	1.9571(1)	1.9488(1)	1.9467(1)
Mn−$O1_{eq}$ (Å) (× 2)	1.941	1.9426(1)	1.9491(2)	1.9518(6)	1.937(1)	1.9392(4)	1.940(2)	1.944(2)
Mn−$O2_{eq}$ (Å) (× 2)	1.900	1.9006(1)	1.9043(2)	1.9071(6)	1.937(1)	1.9391(7)	1.940(2)	1.944(2)
Mn−O_{ap}−Mn (°)	180.0	180.0	180.0	180.0	180.0	180.0	180.0	180.0
Mn−$O1_{eq}$−Mn (°)	163.81 (8)	164.39 (6)	166.52 (7)	168.91 (2)	168.06 (7)	170.82 (2)	171.63 (8)	176.12 (7)
Mn−$O2_{eq}$−Mn (°)	162.42 (4)	162.98 (6)	165.34 (7)	167.69 (3)		168.25 (3)		

[a] The $x = 0$ results are from reference 20.

remains constant. At ≈125 K, a partial structural transition from *I*4/*mcm* to *Fmmm* occurs (Figure 8) that coincides with a magnetic one toward an A-type AFM state which hinders the further development of FM. Thus, at low temperature the $x = 0.3$ and 0.4 compounds exhibit a mixture of FM and AFM, associated with *I*4/*mcm* and *Fmmm* structures respectively, whose temperature dependence of the lattice parameters is shown in Figure 8. The strong competition between these phases is shown by inverse *x* dependences of % of FM and AFM phases and of the *M* values in both magnetic states (Table 2). In fact, the ratios of *I*4/*mcm*-FM to *Fmmm*-AFM are refined to $^2/_3$:$^1/_3$ and $^1/_2$:$^1/_2$ for 0.3 and 0.4, respectively, and the magnetic moments are calculated as 2.6 μ_B ($x = 0.3$ and 0.4) for the FM component and 3.3 μ_B ($x = 0.3$) and 2.6 μ_B ($x = 0.4$) for the AFM one. The higher content of AFM in $x = 0.4$ than in $x = 0.3$ makes the interpretation tricky, but as previously noted numerous parameters ($<r_A>$, σ^2, strains, etc.) compete in this part of the diagram, and it is possible that the interplay of T_N and T_C dependence on *x* may also play a role. Let us make clear that the refinements of such multiphasic samples are not obvious because of the correlations between the scale factors and the magnetic moments. However, the ratio between the FM and AFM phases, associated with different crystallographic phases, can be considered as significant. Moreover, these observations, deduced from the NPD data and consequently corresponding to average phenomena, are coherent with magnetic (see first section) and transport (see Figure 5 for instance) properties and are in agreement with the electron microscopy characterizations (next section). It is also important to note that, at low temperature, the AFM moment refined on the Mn is generally high, and, at least for $x = 0-0.3$, it closely approaches the theoritical value of 3.5 μ_B (Table 2). In the same way, the FM component for $x = 0.3$ and 0.4 is refined to a significantly lower value suggesting that the *I*4/*mcm* phase, which is at present resolution apparently homogeneous as to the crystal structure, is not perfectly magnetically ordered as a whole, but it contains magnetically incoherent inclusions or inter-

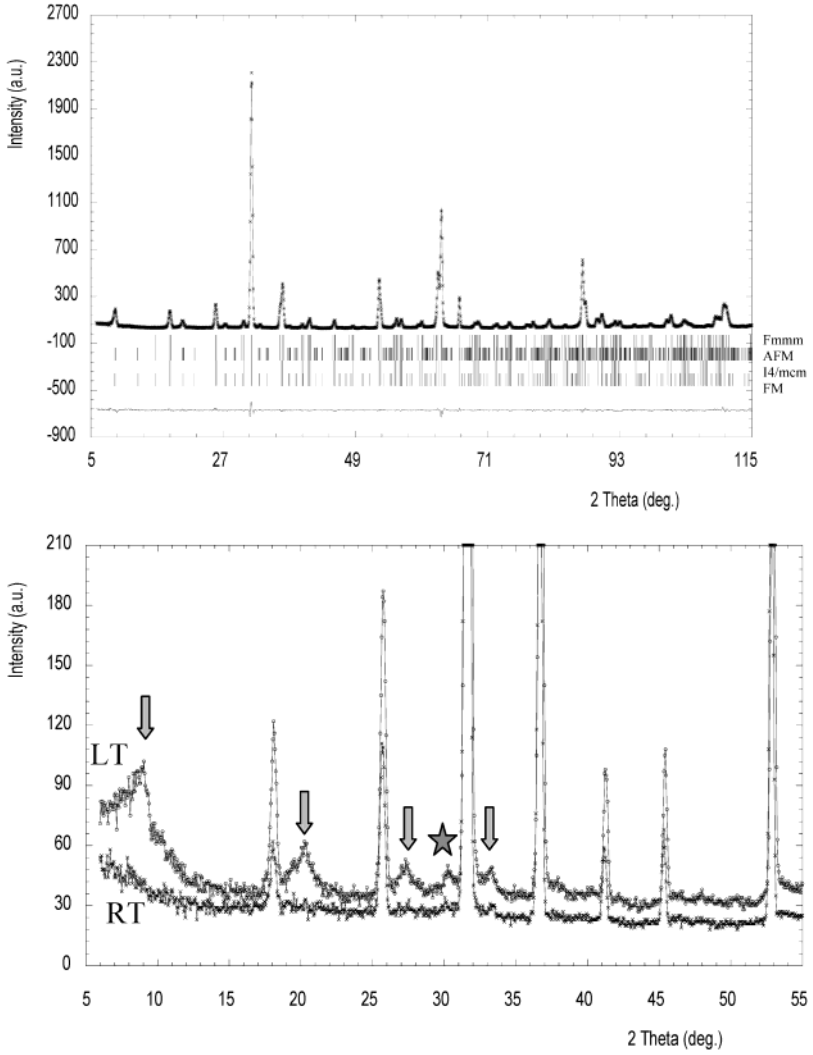

Figure 4. (a) $Pr_{0.5}Sr_{0.1}Ba_{0.4}MnO_3$: 10 K (3T2) NPD refined pattern showing a mixture of *Fmmm* associated with AFM and *I*4/*mcm* corresponding to FM. (b) Comparison between the RT and LT 3T2 NPD patterns (low angles part only) of $Pr_{0.5}Ba_{0.5}MnO_3$. The RT one can be indexed in the *Pm*3*m* space group, and the LT one can be indexed in the *I*4/*mcm* one. The star is for the peak that differentiates *I*4/*mcm* from *Pm*3*m* and the arrows are for the magnetic peaks, characteristic from A-type AFM.

growth of nanoscopic size (PM, AFM, or glassy state). The fraction of these regions increases with x, as confirmed in the following with the $x = 0.5$ sample.

The study of the end composition $Pr_{0.5}Ba_{0.5}MnO_3$ confirms the complexity of this series. In fact, the diagrams registered on G41 as a function of temperature do not show any clear structural transition from 300 K down to 1.5 K. The weak tetragonal distortion determined on the 10 K 3T2 diagram is difficult to detect because of the smaller Q range of the G41 spectrometer compared to that of the 3T2. Nevertheless, the magnetic transitions can be determined: $T_C \approx 140$ K and $T_N \approx 80$ K. Let us now compare the temperature dependence of the lattice parameters for the $x = 0.3$, 0.4, and 0.5 compositions. Figure 8a shows a "two-step transition" to AFM at ≈140 K and ≈110 K, which suggests that the FM phase originating below 140 K is subjected to a strong elastic coupling. With decreasing temperature, the AFM regions grow toward a long range ordering, allowing a proper lattice distortion to develop below 110 K. The lattice parameters for $x = 0.4$ (Figure 8b), comparable to those for $x = 0.3$ between 140 and 110 K, suggest that the stress imposed by the surrounding FM matrix is present down to the lowest temperatures. Finally, for $x = 0.5$ no orthorhombic distortion can be detected in the mixed FM/AFM state at the present experimental resolution, pointing to a still stronger internal stress and therefore nanoscopic nature of AFM intergrowths in this compound. This evolution, vs x, of the magnetic structure and MnO lattice distortion is regular from $x = 0.3$ to 0.5, whereas local cationic order is only evidenced for $x = 0.5$.

III. Electron Microscopy. The $x = 0.05$, 0.3, 0.4, and 0.5 have been characterized by electron microscopy. The detailed study of the $x = 0$ sample, $Pr_{0.5}Sr_{0.5}MnO_3$, has been previously reported for the 92−300 K temperature range.[20] One important point was to investigate the homogeneity of the samples by HREM, especially looking at possible short-range ordering phenomena on the cationic (Pr, Ba, and Sr) sites and/or associated to oxygen displacements or vacant sites. These two types of deviations from the expected random atomic distribution are indeed susceptible to drastically modify the magnetotransport properties. A typical enlarged [$\bar{1}$10] HREM image of the tetragonal $Pr_{0.5}Sr_{0.1}Ba_{0.4}MnO_3$ is given in Figure 9a, where cations positions appear as dark dots. The simulated image calculated for the positional parameters refined from neutron diffraction

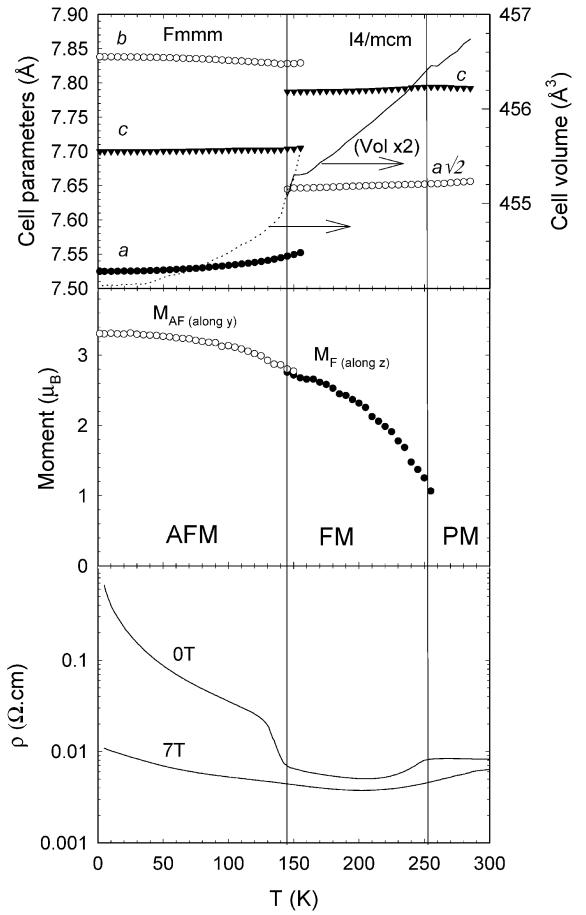

Figure 5. $Pr_{0.5}Sr_{0.45}Ba_{0.05}MnO_3$: from top to bottom - evolution of the cell parameters (left *y*-axis) and lattice volume (right *y*-axis) versus *T*; temperature dependence of the magnetic moment refined from G41 NPD data; and resistivity curves [ρ (T)] with (7 T) or without applied magnetic field.

data (focus value $\Delta f = -80$ nm and crystal thickness $t = 2$ nm) is superimposed on the experimental one, showing a very good fit. The regularity of the contrast and the absence of local modulation are clearly visible. This study confirms the homogeneity of all the samples at room temperature; moreover, the EDS analyses, carried out with different probe diameters (down to 10 nm), show that there is no significant local variation of the cationic composition.

For each of the samples, the reciprocal space was reconstructed at room temperature. The [010] and [$\bar{1}$10] ED patterns of the $Pr_{0.5}Sr_{0.1}Ba_{0.4}MnO_3$ sample are given as examples in Figure 9b and c; the conditions limiting the reflection are *hkl*: $h + k + l = 2n$, consistent with the *I*4/*mcm* space group.

The investigation of the $x = 0.05$ sample vs *T* shows that the structural evolution is similar to that of the $x = 0$ sample.[20] Upon warming the sample from 92 K, the abrupt transition corresponding to the transition from the AFM structure (*Fmmm*) to the FM (*I*4/*mcm*) appears at a temperature close to 140 K. This transition is clearly observed in bright field images by the abrupt disappearance of the twinning domains.[20]

A different behavior is observed for the $x = 0.3$ sample, $Pr_{0.5}Sr_{0.2}Ba_{0.3}MnO_3$. At low temperature, the reflections are split as the result of the *Fmmm* cell distortion. One example of [001] ED pattern recorded at 92 K is given in Figure 10a. However, a careful examination of the reflections shows that they are slightly elongated, and in some grains they are split in several spots as a result of the coexistence of *Fmmm* and *I*4/*mcm* structures. The bright field images (Figure 10b) show that in these latter crystallites areas with twinning domains coexist with untwinned areas. The zone labeled 1 exhibits numerous twin boundaries and is characteristic of the *Fmmm* structure associated with the AFM. In the zone labeled 2 no twin boundary is observed, and the selected area pattern does not show any distortion so that it may be associated to the second phase (*I*4/*mmm*) observed in NPD. Warming the sample from 92 K, the disappearance of the twinning domains is observed at about 125 K. The difference with the Sr-rich phases deals with the fact that above 125 K the reflections are not sharp but are cross shaped, with the arms pointing along the [100]* and [010]* of the tetragonal *I*4/*mcm* cell (Figure 10c), and the bright field images exhibit a tweed-like structure characteristic of a phase transition and generated by the strain effect due to the coexistence of the two phases.[24] At 160 K, all these effects have disappeared and the ED patterns and the bright field images are characteristic of the room-temperature phase. These phenomena can be interpreted by the nucleation of the distorted *Fmmm*-type phase in the *I*4/*mcm*-type matrix at 160 K (decreasing *T*), they coexist and evolve in the 150−110 K temperature range, and last, at 120 K, a phase segregation is observed with the formation of large *Fmmm*- and *I*4/*mcm*-type domains (from a few tenths μm to a few μm wide).

For the $x = 0.4$ sample, $Pr_{0.5}Sr_{0.1}Ba_{0.4}MnO_3$, no *Fmmm*-type distortion has been detected at 92 K. All the crystallites exhibit ED patterns with the cross shaped reflections (Figure 11a) characteristic of the transition state. The bright field images recorded at 92 K (Figure 11b) exhibit the speckled contrast of a constrained material. As for $x = 0.3$, these observations fit with the results of the NPD study (Figure 8).

The RT characterization of $Pr_{0.5}Ba_{0.5}MnO_3$ shed light on the *Pm*3*m* structure deduced from the NPD refinement. The electron microscopy clearly shows that the structure is in fact complex, as previously reported in the $Pr_{1-x}Ba_xMnO_3$ series, around $x \approx 0.5$.[25] The system of intense reflections observed in the RT ED patterns is indeed characteristic of the simple perovskite unit cell, but the shape of the spots and the presence of weak extra reflections reveal that the actual symmetry is locally lower (Figure 12a). The extra reflections are observed in $00^1/_2$ position (see white arrows in Figure 12a), inducing a tetragonal cell with $a = a_p$ and $c = 2a_p$, similar to those observed in the $LaBaMn_2O_5$ perovskites.[26] These oxides are characterized by a cationic ordering, in the form of Ba and La alternative layers, associated with ordered oxygen vacancies, which results from the large difference between the Ba^{2+} and La^{3+} cations. In the [100] ED patterns, these satellites are observed along the three equivalent directions of the perovskite subcell and their intensities vary depending

(25) Barnabé, A.; Millange, F.; Maignan, A.; Hervieu, M.; Raveau, B. *Chem. Mater.* **1998**, *10*, 252.
(26) Millange, F.; Caignaert, V.; Domenges, B.; Raveau, B. *Chem. Mater.* **1998**, *10*, 1974.

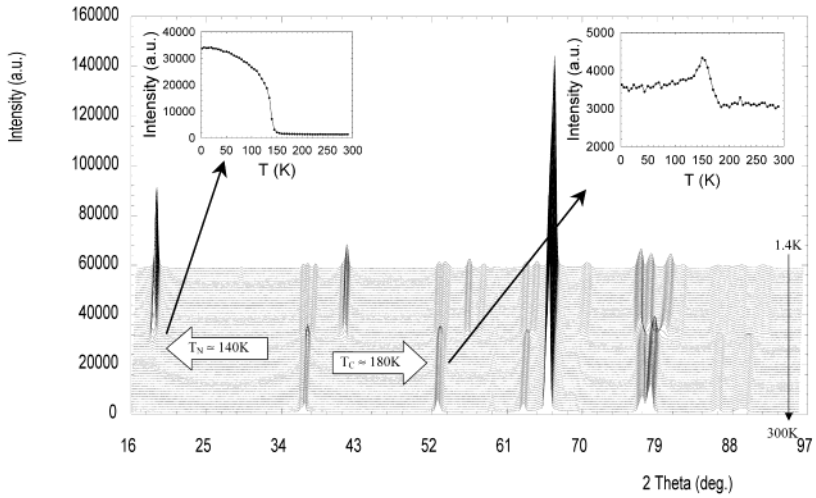

Figure 6. $Pr_{0.5}Sr_{0.3}Ba_{0.2}MnO_3$: evolution of the G41 NPD patterns recorded from 1.5 to 300 K, showing clearly a structural transition associated with the magnetic transition at T_N. Insets give the integrated intensities, vs T, of two peaks characteristic of AFM (left inset) and FM (right inset).

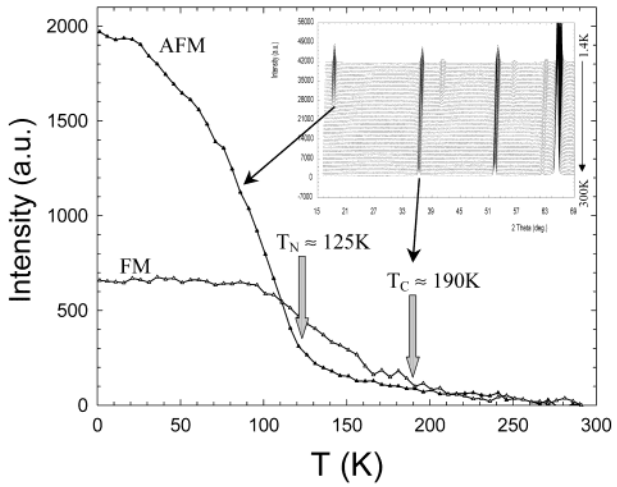

Figure 7. $Pr_{0.5}Sr_{0.1}Ba_{0.4}MnO_3$: determination of the magnetic transition temperatures from the temperature dependence of the integrated intensity of two peaks, taken from the G41 NPD patterns given in inset.

on the selected area. The HREM images (Figure 12b) show that the superstructure is only observed over small domains, 90° oriented, in the perovskite matrix (see white arrows). It can be seen that the maximum size of the ordered domains is a few nanometers. The small size of the ordered domains and the presence of all possible variants explain that they are not detected by neutron diffraction, which leads to an average cubic cell. One important point is to know if a random distribution in such a system (two A-site cations with a large size difference, in the 1:1 ratio) can be stabilized by varying the synthesis conditions. Decreasing the temperature to 92 K, the ED patterns remain unchanged (i.e., no structural transition is observed) but they are characteristic of a strained structure. Such an evolution vs temperature was also previously reported for $Ho_{0.5}Sr_{0.5}MnO_3$,[27] another half-doped manganite that also exhibits a large σ^2 but a small $<r_A>$. At low temperature, for both compounds ($Pr_{0.5}Ba_{0.5}MnO_3$ and $Ho_{0.5}Sr_{0.5}MnO_3$), the large σ^2 makes A-type AFM to order only at short

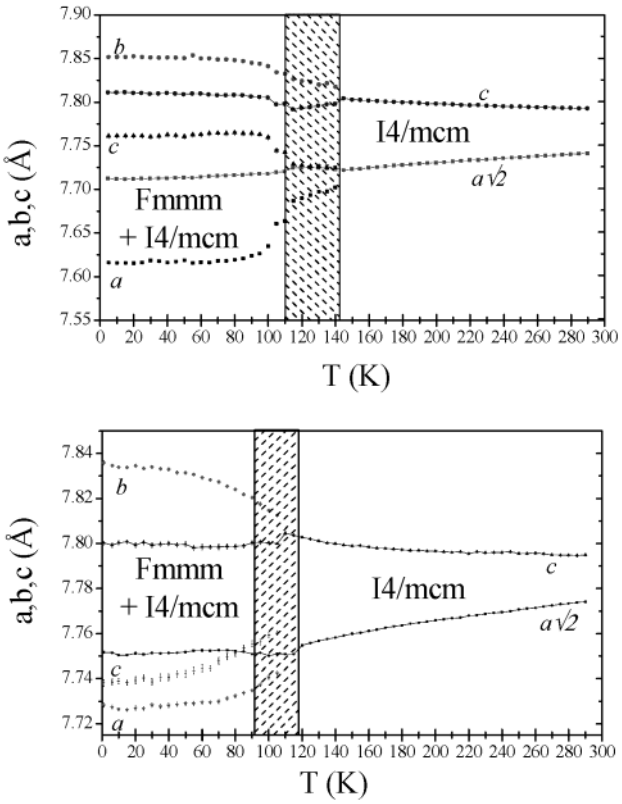

Figure 8. Temperature dependence of the lattice parameters observed for (a) $Pr_{0.5}Sr_{0.2}Ba_{0.3}MnO_3$ and (b) $Pr_{0.5}Sr_{0.1}Ba_{0.4}MnO_3$ (from G41 NPD data). The hatched zones indicate the transition areas where the accuracy of the fits is not good, because the transitions take place progressively.

range, in connection with the strained structures. Due to its large $<r_A>$, at low temperature, a structure with Mn−O−Mn angles of ≈180° is observed for $Pr_{0.5}Ba_{0.5}MnO_3$ that also exhibits FM, whose existence leads to MR properties. In contrast, for $Ho_{0.5}Sr_{0.5}MnO_3$, the small $<r_A>$ favors a strongly distorted MnO framework that does not allow FM to develop.

Discussion

The first important point is that, through the entire series, the good agreement evidenced between first NPD

(27) Autret, C.; Martin, C.; Maignan, A.; Hervieu, M.; Raveau, B.; André, G.; Bourée, F. *J. Solid State Chem.* **2002**, *165*, 65.

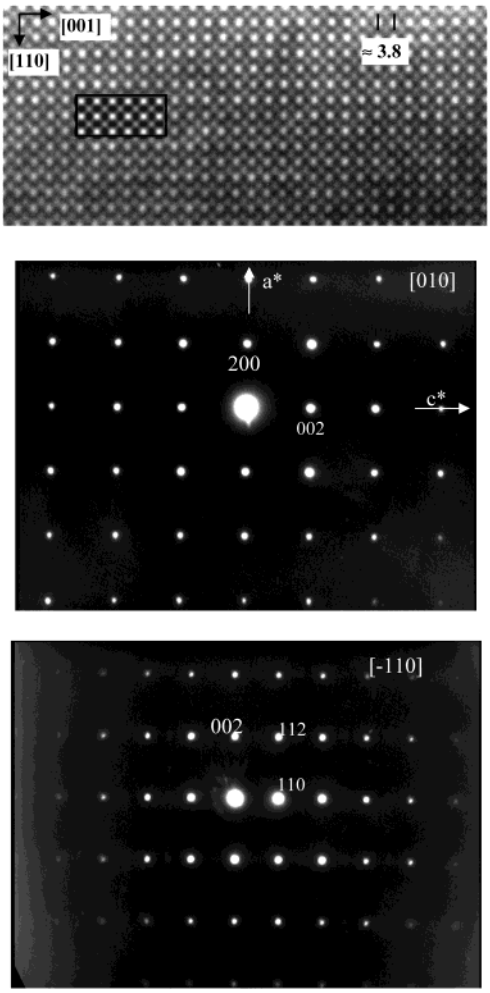

Figure 9. $Pr_{0.5}Sr_{0.1}Ba_{0.4}MnO_3$ at room temperature: (a) typical [1 $\bar{1}$0] HREM image and simulation, showing the even contrast; (b) [$\bar{1}$10]; and (c) [010] ED patterns.

results and electron microscopy observations and then between structural behaviors and magnetic properties allows a better understanding of this complex system. For instance, the particular low temperature state evidenced by NPD for the larger x values compounds is correlated with the electron microscopy versus temperature study and explains the magnetization curves. On the other hand, the magnetic transitions observed on the magnetization curves (Figure 1) fit with those determined from the NPD patterns (Figure 5, 6, or 7). The correlations between structural, magnetic, and electric properties, examplified in Figure 5 for the $x = 0.05$ compound, show the strong interplay between structures and properties in the manganites.

Two space groups are mainly involved in this $Pr_{0.5}Sr_{0.5-x}Ba_xMnO_3$ series: $I4/mcm$ and $Fmmm$. Only the end member $Pr_{0.5}Ba_{0.5}MnO_3$ exhibits a cubic structure (zero-tilt system) at RT due to the large average A-site cationic size, but as seen by electron microscopy, the structure is constrained and locally of lower symmetry, in connection with short-range cationic order. The difficultyof obtaining a pure cubic structure for this composition was previously reported.[25] The other compounds are of the $I4/mcm$ type in the PM state at RT. They thus exhibit a one-tilt perovskite system ($a^0a^0c^-$ in the Glazer notation[28,29]) that is retained at LT, even when the samples become AFM, and because of associated tetragonal contraction of the MnO_6 octahedra, acquire the $Fmmm$ symmetry. In a general way, at RT the structure is more distorted for the small x values, and moreover, at decreasing temperature, the distortion is more pronounced for these small x samples. This leads for the large x values to complex states with mixtures of phases with closely related structures. From this point of view, it is interesting to follow the x dependence of the structure associated with the A-type AFM order. For the compositions close to $Pr_{0.5}Sr_{0.5}MnO_3$, the usual

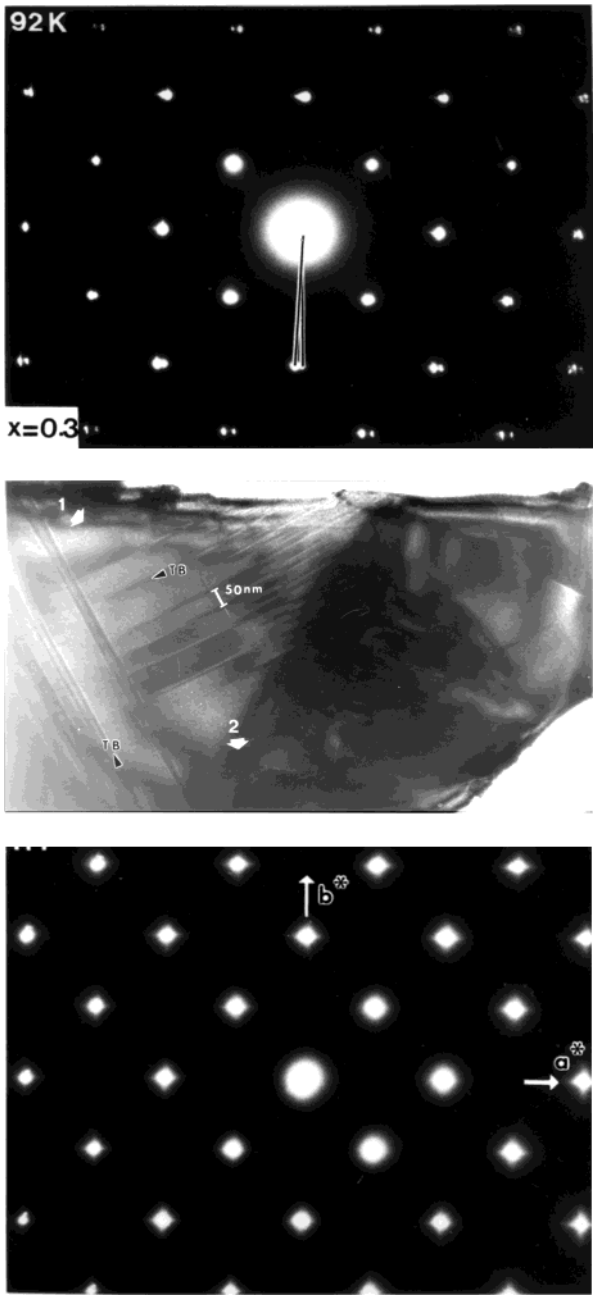

Figure 10. $Pr_{0.5}Sr_{0.2}Ba_{0.3}MnO_3$ at 92 K: (a) [001] ED pattern, the two lines evidence the splitting of the 220 reflection (indexation in a $Fmmm$ cell); and (b) [001] bright field image. Twinning domains are observed only in zone 1; (c) [001] ED of $Pr_{0.5}Sr_{0.2}Ba_{0.3}MnO_3$ recorded at 140 K.

(28) Glazer, A. M. *Acta Crystallogr. B* **1972**, *28*, 3384.
(29) Woodward, P. M. *Acta Crystallogr. B* **1997**, *53*, 32.

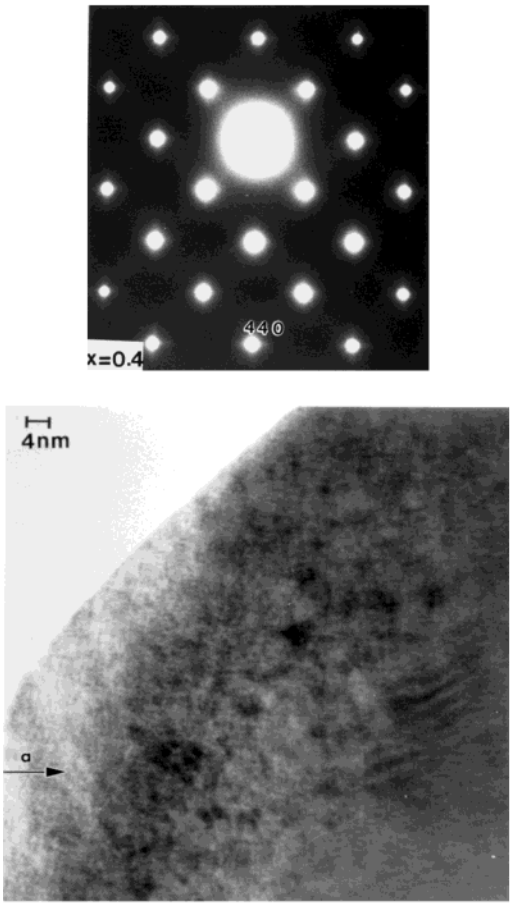

Figure 11. $Pr_{0.5}Sr_{0.1}Ba_{0.4}MnO_3$ at 92 K: (a) [001] ED pattern (the indexation is made in the F-type cell to be directly compared with Figure 10a where the splitting of the 440 is clearly observed); and (b) [001] bright field image showing the speckled contrast due to the strain effect.

distortion associated with the A-type AFM, that is a Mn−O distance clearly shorter than the two others, is evidenced. For the large $<r_A>$ and σ^2 samples, even if the A-type AFM is visible at long range on the NPD patterns, the refined average cell does not allow such a distortion to be evidenced. This leads, for $Pr_{0.5}Ba_{0.5}MnO_3$, to a nearly cubic structure associated with a short range A-type AFM. This shows the ability of such perovskite manganites to stabilize A-type AFM in a nearly cubic structure. This result is also in agreement with electronic structure calculations for half-doped A-type manganites showing that the A-type phase remains stable even if the lattice is not allowed to develop a proper distortion, e.g., due to internal stress imposed by the two-phase coexistence at nanoscopic level and/or the short-range cationic.[30]

This work dealing with the $Pr_{0.5}Sr_{0.5-x}Ba_xMnO_3$ system was mainly motivated by completing our first neutron diffraction investigation of the $Pr_{0.5}Ca_{0.5-x}Sr_xMnO_3$ series[7] and particularly to study the mismatch effect in this half-doped system. In fact, as shown Figure 13, starting from $Pr_{0.5}Ca_{0.5}MnO_3$ the average A-site cationic size increases with the Sr content and then the Ba content, and the mismatch that characterizes the A-site size difference effect increases more quickly for

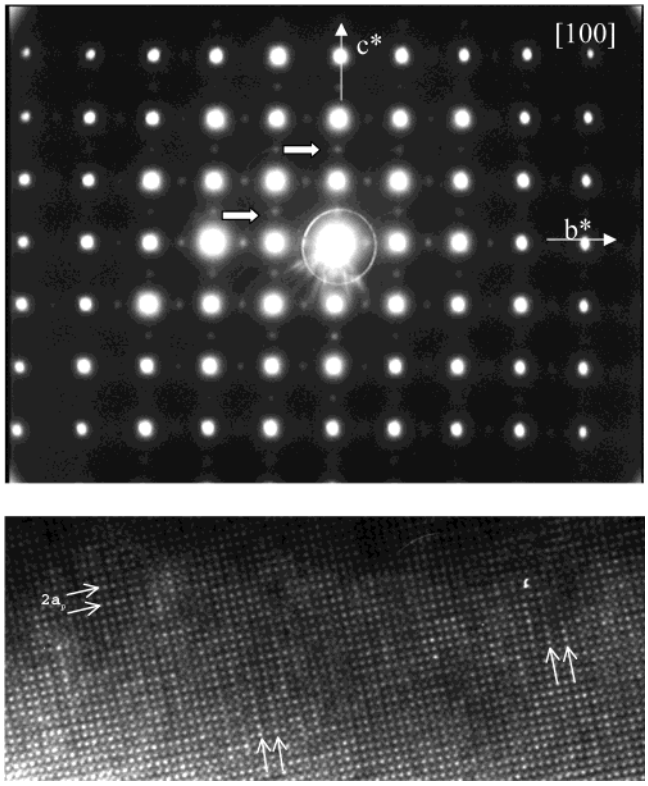

Figure 12. $Pr_{0.5}Ba_{0.5}MnO_3$ at RT: (a) [100] ED pattern; and (b) HREM image.

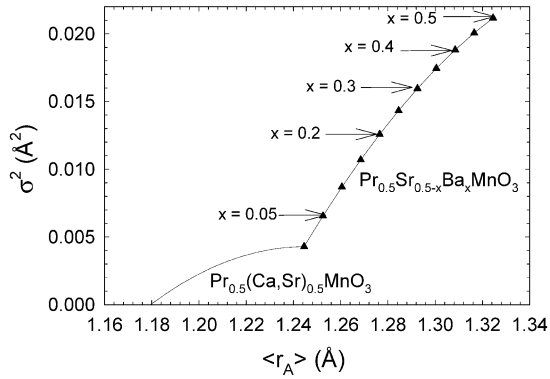

Figure 13. Plot of σ^2 vs $<r_A>$ for the $Pr_{0.5}Sr_{0.5-x}Ca_xMnO_3$ and $Pr_{0.5}Sr_{0.5-x}Ba_xMnO_3$ series, the x values are given for the latter.

the second series than the first one. It explains for instance that the synthesis conditions have to be well controlled to avoid, for the larger Ba contents, the formation of hexagonal phases[14,15] or of ordered phases (due to cationic, Ba/Pr, or anionic, oxygen/vacancies, ordering).[26,31,32] It is thus possible to enlarge the previously published magnetic phase diagram[7] toward the larger $<r_A>$. Let us make clear that this diagram was elaborated from the NPD data, and that for this $Pr_{0.5}Sr_{0.5-x}Ba_xMnO_3$ series, as previously discussed, the behaviors vs. T are very often complex. Because of broad transitions or coexistence of several background states, or both, it is difficult to schematize these features in a simple picture. Consequently Figure 14 has to be taken as only a simplified phase diagram that can be described

(30) Fang, Z.; Solovyev, I. V.; Terakura, K. *Phys. Rev. Lett.* **2000**, *84*, 3169.

(31) Troyanchuck, I. O.; Trukhanov, S. V.; Szymczak, H.; Baerners, K. *J. Phys. Condens. Matter.* **2000**, *12*, L155.

(32) Trukhanov, S. V.; Troyanchuck, I. O.; Vita, I. M.; Szymczak, H.; Bärner K., *J. Magn. Magn. Mater* **2001**, *237*, 276.

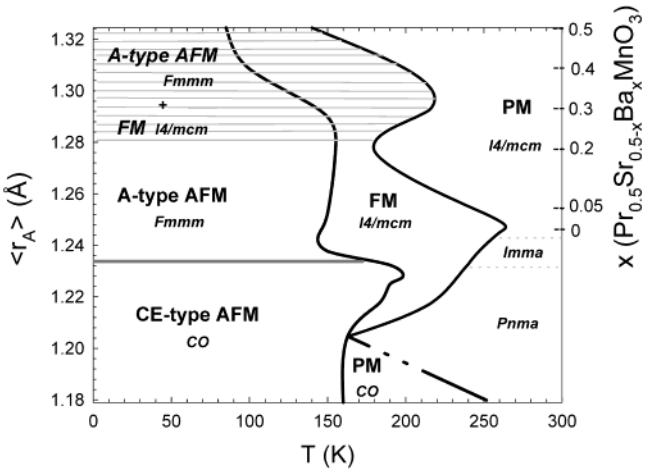

Figure 14. Schematized ($<r_A>$, T) magnetic phase diagram, from NPD data, corresponding to the half-doped $Pr_{0.5}Sr_{0.5-x}Ca_xMnO_3$ (lower part of the picture) and $Pr_{0.5}Sr_{0.5-x}Ba_xMnO_3$ (upper part) systems. The x values corresponding to the samples studied by NPD in the latter series are also given (right y-axis). The hatched area is to illustrate the fact that in the upper part of the diagram ($x > 0.2$) the samples are never totally magnetically ordered.

by the following six zones: (i) All the compounds are in the PM state at RT and the structure evolves from *Pnma* to *Imma* and then *I*4/*mcm* by increasing $<r_A>$. The ortho-tetragonal boundary is at $<r_A> \approx 1.235$ Å. (ii) In a small area, manganites with compositions close to $Pr_{0.5}Ca_{0.5}MnO_3$ exhibit a charge ordered (CO) PM state. (iii) A large part in the middle of the diagram corresponds to FM associated with the *I*4/*mcm* space group; note that for the large Ba contents it is not pure FM, with the FM phase content being well below 100%. (iv) At LT, for the small $<r_A>$, the oxides are CE-type AFM and CO. (v) For intermediate $<r_A>$, the LT form is A-type AFM and the space group is *Fmmm* (prototype: $Pr_{0.5}Sr_{0.5}MnO_3$). (vi) The LT state observed for the larger $<r_A>$ is complex with a mixture of FM and AFM, moreover, a large part of the compound is not well magnetically ordered.

From $Pr_{0.5}Sr_{0.5}MnO_3$ to $Pr_{0.5}Sr_{0.3}Ba_{0.2}MnO_3$, by decreasing temperature, three magnetic states are observed PM/FM/AFM with a decrease of the T_C whereas T_N remains nearly constant. This evolution is attributed to the increase of σ^2 that counterbalances the increase of $<r_A>$ which generally favors ferromagnetism. In fact, comparing various series, it was previously reported[18] that $Pr_{0.5}Sr_{0.5-x}Ba_xMnO_3$ (with $x \leq 0.2$) was the only system where the mismatch effect becomes preponderant upon the mean size effect. Then for $x > 0.2$, a strong competition between FM and AFM is observed, even at low temperature leading to a large multiphasic zone. An important point is that this phase separation allows the Curie temperature to be increased. Note also that for these $x > 0.2$ compounds, for intermediate temperatures where only FM occurs or at lower temperatures where FM and AFM coexist, the calculated magnetic moments are much lower than the theoretical ones, demonstrating that the higher mismatch values tend to weaken the magnetic interactions. This point is confirmed by the study of samples that exhibit different σ^2 values for a same $<r_A>$.[33] In this series, $Pr_{0.5}Ba_{0.5}MnO_3$ exhibits a particular behavior with local cationic ordering, short-range A-type AFM, and a large fraction of poorly magnetically ordered component, even at low temperature. This complex state is associated with unusual properties which will be separately reported.[34]

Conclusion

This study shows the great complexity of the $Pr_{0.5}Sr_{0.5-x}Ba_xMnO_3$ system that forms a very rich system from the structural and magnetic points of view, governed by the A-site size and size mismatch, two key parameters whose effects are antagonistic. These results, together with those previously reported for $Pr_{0.5}Ca_{0.5-x}Sr_xMnO_3$, show the connection between the magnetic and structural parameters and the properties.

Two original features must be emphasized from the observation of the magnetic phase diagram. The first one concerns the ability of this system to exhibit, for large $<r_A>$ and σ^2 values, at low temperature, phase separation into AFM, FM, and poorly ordered magnetic phases.

The second original feature deals with the evidence, for large σ^2 values, of A-type AFM that orders only at short range, as previously reported for $Ho_{0.5}Sr_{0.5}MnO_3$. But for the large $<r_A>$ values (i.e., for $Pr_{0.5}Ba_{0.5}MnO_3$), it develops in a nearly cubic structure similar to the FM phase.

CM020474S

(33) Autret, C.; Maignan, A.; Martin, C.; Hervieu, M.; Raveau, B. Submitted for publication.

(34) Autret, C.; Maignan, A.; Martin, C.; Hervieu, M.; Hardy, V.; Hébert, S.; Raveau, B. *Appl. Phys. Lett.* Submitted for publication.